



Review

# Progress in Hexagonal Boron Nitride (h-BN)-Based Solid-State Neutron Detector

Samiul Hasan \* and Iftikhar Ahmad

Department of Electrical Engineering, University of South Carolina, Columbia, SC 29208, USA; ahmad@cec.sc.edu  
\* Correspondence: shasan@email.sc.edu

**Abstract:** This article will briefly review the progress of h-BN based solid-state metal semiconductor metal (MSM) neutron detectors. In the last decade, several groups have been working on hexagonal boron nitride (h-BN)-based solid-state neutron detectors. Recently, the detection efficiency of 59% has been reported. Efficient, low-cost neutron detectors made from readily available materials are essential for various applications. Neutron detectors are widely used to detect fissile materials and nuclear power plants for security applications. The most common and widely used neutron detectors are  $^3\text{He}$  based, which are sometimes bulky, difficult to transport, have high absorption length, need relatively high bias voltage ( $>1000\text{ V}$ ), and have low Q-value (0.764 MeV). In addition,  $^3\text{He}$  is not a readily available material. Thus, there is a strong need to find an alternative detection material. The  $^{10}\text{B}$  isotope has a high neutron absorption cross-section, and it has been tested as a coating on the semiconducting materials. Due to the two-step process, neutron capture through  $^{10}\text{B}$  and then electron-hole pair generation in a typical semiconducting material, the efficiency of these devices is not up to the mark. The progress in h-BN based detectors requires a review to envision the further improvement in this technology.

**Keywords:** h-BN; neutron detector; solid-state detector; metal semiconductor metal



**Citation:** Hasan, S.; Ahmad, I.

Progress in Hexagonal Boron Nitride (h-BN)-Based Solid-State Neutron Detector. *Electron. Mater.* **2022**, *3*, 235–251. <https://doi.org/10.3390/electronicmat3030020>

Academic Editor: Wojciech Pisula

Received: 27 April 2022

Accepted: 19 July 2022

Published: 3 August 2022

**Publisher's Note:** MDPI stays neutral with regard to jurisdictional claims in published maps and institutional affiliations.



**Copyright:** © 2022 by the authors. Licensee MDPI, Basel, Switzerland. This article is an open access article distributed under the terms and conditions of the Creative Commons Attribution (CC BY) license (<https://creativecommons.org/licenses/by/4.0/>).

## 1. Introduction

Neutrons are electrically neutral and indirect ionizing radiation [1]. They are mainly generated from nuclear fission reactions but can also be the signature of the presence of particular types of radioactive materials. The penetration depth of neutrons is large due to their charge neutrality and low mass compared to other nuclear particles. When a neutron interacts with matter, three types of events can happen [1]: elastic scattering, inelastic scattering, and radiative absorption. Both high-energy ( $\approx 1\text{--}2\text{ MeV}$ ) fast neutron (elastic scattering event) and low-energy ( $\approx 0.025\text{ eV}$ ) thermal neutron (radiative absorption event) interactions are current research topics for developing neutron detectors [2]. Highly efficient neutron detectors are essential for various applications such as oil borehole logging, neutron forensics, fissile material sensing, etc. [3,4]. The thermal neutrons are usually detected indirectly using a conversion medium [5]. Neutrons absorbing isotopes with a high microscopic neutron absorption cross-section act as the conversion medium. These isotopes release ionizing radiation such as gamma rays or charged particles upon the absorption of neutrons [6]. Different isotopes are used as neutron-absorbing media such as  $^3\text{He}$ ,  $^6\text{Li}$ ,  $^{10}\text{B}$ ,  $^{113}\text{Cd}$ ,  $^{235}\text{U}$ ,  $^{135}\text{Xe}$ , and  $^{199}\text{Hg}$ , where their neutron-absorbing cross-sections are diverse, as shown below [7].

Feasible materials can be used as a coating material in the direct semiconducting material [8,9]. The isotopes having a high neutron absorption cross-section and low atomic mass to absorb thermal neutrons are preferable due to scattering [10]. Currently,  $^3\text{He}$  is the most widely used material, but it has limitations such as high bias voltage, high cost, and scarcity [11–17]. We observe in Table 1 that the neutron absorption cross-section of  $^3\text{He}$  is  $\approx 5333$  barns, which is higher than  $^{10}\text{B}$  (3838 barns) [8]. However, the atomic density of  $^{10}\text{B}$  in hexagonal boron nitride (h-BN) is higher than  $^3\text{He}$ ; thus, the thermal neutron absorption

coefficient is much higher [18]. It has been shown in the previous works that  $^{10}\text{B}$  can be a prospective replacement of  $^3\text{He}$  [19]. The reaction due to thermal neutron capture in  $^{10}\text{B}$  can be written as shown in Equations (1) and (2) [20]:

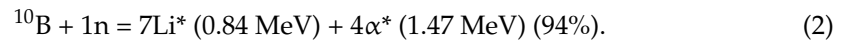
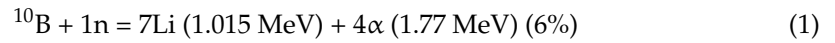


**Table 1.** Thermal neutron absorption cross-section for different isotopes [7].

Isotope	Cross Section in Barn (1 barn = $10^{-24} \text{ cm}^2$ )
$^3\text{He}$	5333
$^6\text{Li}$	941
$^{10}\text{B}$	3838
$^{113}\text{Cd}$	20,600
$^{235}\text{U}$	681
$^{135}\text{Xe}$	2,720,000
$^{199}\text{Hg}$	2150

The  $^{10}\text{B}$  isotope enriched coating layer works as a neutron to alpha particle conversion medium on semiconductors (Si/GaAs) but has very low efficiency (2–5%) due to a two-step process [21–27]. The coating material needs to be thick so that enough neutrons can be absorbed. However, the problem is that the by-products of the reaction mentioned above, Li and alpha ions, can travel only 2–5  $\mu\text{m}$ . Thus, this process cannot generate enough corresponding electron–hole pairs in the semiconducting materials due to the low diffusion length of Li atoms and alpha ions [28,29]. Other candidates such as  $\text{B}_4\text{C}$  and pyrolytic boron nitride-based detectors are still suffering design issues and low detection efficiency [30]. Other challenges include material quality, collection of charges before recombination, etc. [31]. h-BN has been researched and developed for the last 10–15 years as a prospective semiconductor neutron detector material despite all these shortcomings. An external bias pushes the created electron–hole pairs in the semiconductor material toward the anode and cathode, generating an electrical signal [32]. This signal passed through external circuit elements, which are characterized by a multichannel analyzer (MCA) [32]. Thus, a semiconductor material acts as a neutron detector. Generally, semiconductor materials need to have certain properties to act as radiation detectors such as a large bandgap, high resistivity, small electron–hole pair energy, high material quality, low dielectric constant, high radiation hardness, and high thermal conductivity [33]. Note that the large bandgap and small electron–hole pair energy are opposite to each other. The electron–hole pair energy is proportional to the bandgap energy. A large bandgap energy is essential to have a low leakage current and low noise, especially when applying a high bias voltage to detect low energy radiation. Small electron–hole pair energy ensures that a high number of electron–hole pairs are generated for an ionizing radiation so that the radiation signal to noise ratio is high. Based on the criteria mentioned above, Table 2 compares existing semiconductor-based radiation detector materials with h-BN.

**Table 2.** Physical parameters comparison for different semiconductor materials [34–36].

Material	Si	Ge	CdTe	$\text{Cd}_{0.5}\text{Zn}_{0.5}\text{Te}$	4H SiC	a-Se	h-BN
Crystal structure	Cubic	Cubic	Cubic	Cubic	Hexagonal	Amorphous	Hexagonal
Production method	CZ	CZ	THM	BM, THM	PVT-Bulk, CVD-epitaxy	HVTE-Thin film	MOCVD
Atomic number	14	32	48,52	48,30,52	14,6	34	5,7
Density	2.33	5.33	6.2	5.78	3.21	6.4	2.18
Bandgap	1.12	0.67	1.5	1.6	3.27	2.24	~6.4
Dielectric constant	11.7	16.2	10.2	~11	9.7	~6	4.9
e-h pair creation energy	3.62	2.96	4.43	4.6	7.28	~50	18
Resistivity	$10^4$	50	$10^9$	$>10^{10}$	$>10^{12}$	$\sim 10^{13}$	$\sim 10^{13}$

CZ = Czochralski, THM = Traveling Heater Method, BM = Bridgman Method, PVT = Physical Vapor Transport, CVD = Chemical Vapor Deposition, HVTE = Halide Vapor Transport Epitaxy, MOCVD = Metal–Organic Chemical Vapor Deposition.

Based on the material properties in Table 2, h-BN can be an ideal candidate to compete with existing commercialized thermal neutron detectors. It has a large bandgap compared to other radiation detector materials, so the radiation detectors prepared with h-BN will have low thermal noise. The high resistivity compared to other materials makes h-BN-based detectors have low leakage current [37–39]. h-BN is reported to be grown by metal–organic chemical deposition (MOCVD) systems; thus, the growth process is robust, controllable, and produces less defective material. Li et al. showed a comparative chart in 2011 showing the feasibility of h-BN (Table 3) as a neutron detector, and they mentioned defect-free epitaxial growth as a challenge [31].

**Table 3.** Neutron detector-type comparison (Reprinted/adapted with permission from Ref. [31]. Copyright 2011, Elsevier).

	$^3\text{He}$	Scintillator Detector	B Coated Detector	BN Semiconductor Detector
Particle generated by neutron	ions	photons	Ions, electrons, holes	Ions, electrons, holes
Active thickness	$\approx 10$ cm	$\approx 1$ mm	$\approx 100$ $\mu\text{m}$	$\approx 100$ $\mu\text{m}$
Key issue	Shortage of $^3\text{He}$ gas	sensitivity	sensitivity	Suitable materials
Response speed	$\approx 1$ ms	$\approx 1$ ns	$\approx 1$ ns	1 ns
Intrinsic detection efficiency	high	Low	Low	High
Cost	High	Low	Low	Low
Portability	Poor	Medium	High	high

The objective of this paper is to review the recent progress and challenges in the development of h-BN based metal semiconductor metal (MSM) thermal neutron detectors. In the first part of the article, we have described the h-BN structure, growth process, and fabrication. After that, we will review the results of the fabricated devices to date and their shortcomings. Our discussion will conclude with some perceived future work for commercializing these detectors.

## 2. Materials and Methods

h-BN is a group III–V semiconductor with boron and nitrogen atoms bonded one after another. The two  $sp^2$  bonded layered configuration is very similar to hexagonal graphite. Figure 1 shows the atomic structure of h-BN, where one nitrogen atom sits next to a boron atom. Atoms in the same plane are strongly  $sp^2$  bonded as a sheet, and the weak Van der Waals interaction attracts these sheets [40]. h-BN is a wide bandgap material, as mentioned in Table 1. The first principle calculation showed an interesting phenomenon reported by Jin Li et al. [41]. Their density functional theory-based calculations showed that the bandgap is a function of symmetrical compressive strain and asymmetrical tensile strain, which can create transitions of direct bandgap to indirect bandgap property.

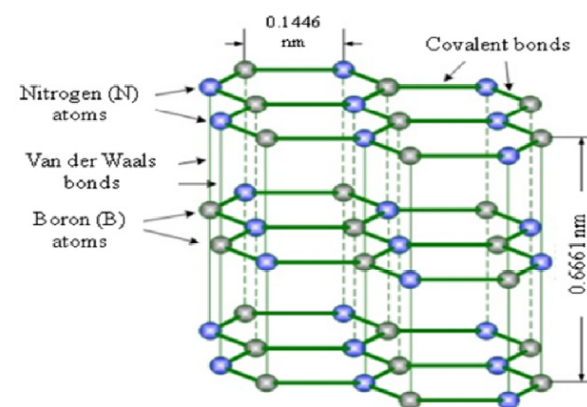


**Figure 1.** h-BN stacked structure (the image is reproduced from [40], copyright 2012, with permission from SPIE).

The experimental fabrication process for the h-BN based neutron detector is illustrated in Figure 2, as mentioned in reference [32].



**Figure 2.** Schematic of h-BN detector fabrication process.

### 2.1. Growth of h-BN

The synthesis of h-BN can be classified into two different approaches: top-down and bottom-up. Figure 1 shows that h-BN has a 2D graphite-like structure with interlayer Van der Waals interactions [42,43]. These weak interactions can be easily overcome by shear forces, mechanical exfoliation, or ball milling procedures [44–48]. The problems with these top-down methods are the limited yield and small flake size. The liquid exfoliation method can be considered another alternative to breaking the interlayer van der Waals forces [47,49,50]. Compared to graphene, where mechanical exfoliation is much more common, h-BN is less popular for this method, as the interlayer interaction is much stronger in the case of h-BN [45,47,48,51]. The top-down approaches are easy to handle compared to the bottom-up approaches, but it is hard to control the thickness, size of the flakes, and surface contamination. The bottom-up approaches can be adopted with or without a substrate. h-BN nanosheets can be grown without substrate by direct chemical reactions of precursor in the wet medium [46,52,53]. Deposition techniques such as low-pressure chemical vapor deposition (CVD), catalytic CVD, plasma-enhanced CVD, and ion beam deposition are the most common bottom-up approaches [51,54–56]. CVD is a low-cost, easily controlled growth technique for the III-nitride material system, especially h-BN [57,58]. There are a couple of controllable growth parameters to produce high-quality, large area, single-crystalline layered structures. The typical CVD set up is added in the Supplementary Figure S1.

Recently, Metal–Organic Chemical Vapor Deposition (MOCVD) has been used due to less toxicity and precise control of the precursors [19,59–62]. The most important parameters that have been optimized in the case of MOCVD growth of h-BN are the metal–organic precursors flow rate, growth temperature, type of carrier gas, reactor pressure, etc. [41,63–69]. h-BN has a high melting temperature ( $\approx 3000$  °C), so growth requires a high temperature [70,71]. Typically, for detector applications, h-BN is grown on sapphire. First, a low temperature ( $\approx 800$  °C) buffer layer is grown; then, the main thick detector layer is grown. The typical growth temperature for h-BN is in the range of 1300 to 1500 °C. Usually, the on-shelf trimethylboron (TMB)/triethylboron (TEB) is used as the metal–organic precursor, containing 20%  $^{10}\text{B}$  and 80%  $^{11}\text{B}$ . Ammonia is usually the precursor for nitrogen in the h-BN growth process. The flow rates of the precursors are precisely controlled through mass flow controllers. The growth procedure is usually completed with a pulsed epitaxy sequence where the boron and the nitrogen precursors (triethylboron and  $\text{NH}_3$ ) are alternately supplied to the growth chamber to form thick films. In this process, pulse duration and their numbers are varied to obtain the optimized growth conditions [59,70,71]. The chamber pressure throughout the growth remains constant at  $\approx 10$ –40 torr [58,66,67], and X-ray diffraction methods are used to determine the crystallinity/quality of the h-BN sample [67,72–75]. Figure 3 shows data for a typical h-BN high-resolution X-ray diffraction scan [18]. The radial ( $2\theta$ - $\omega$ ) and angular ( $\omega$ ) scan is usually used to match the lattice parameters and calculate the defect levels from the X-ray diffraction pattern. So far, at (0 0 0 2) reflection, the minimum full-width-at-half-maxima (FWHM) of 385 arcsec has been reported [76].

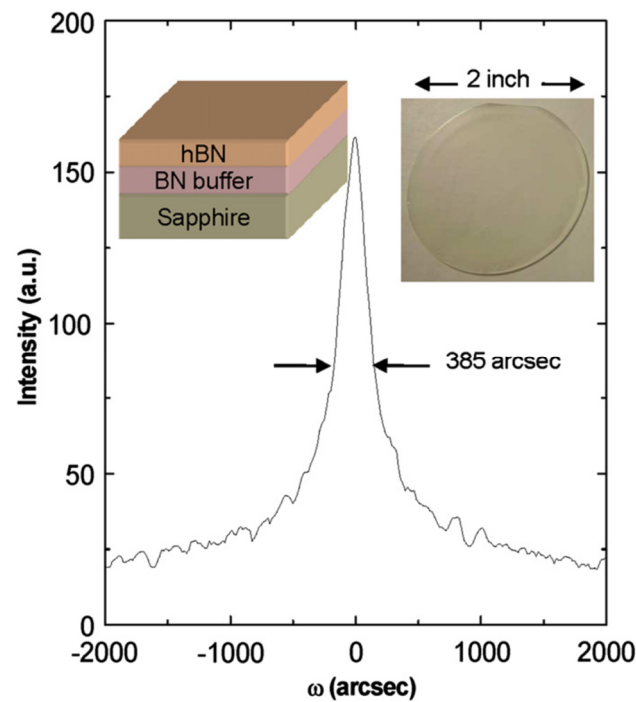


**Figure 3.** Angular scan to find out FWHM (the image is reproduced from [31], copyright 2011, with permission from Elsevier).

The summary of MOCVD-based growth methods is presented in Table 4.

**Table 4.** Growth methods for h-BN.

Precursors	Substrate	Carrier Gas	Growth Temp. (°C)	Pressure (Torr)	Film Quality	Ref.
Triethylamine borane and ammonia (V/III ratio varied between 450 and 2700)	C-plane sapphire (varying surface nitridation)	H <sub>2</sub>	900 (nitridation temperature) 1100 (growth temperature)	20 torr	Good epitaxy achieved	[61]
Pulse mode injection of precursors triethylamine borane and ammonia	C-plane sapphire substrate	H <sub>2</sub>	1350	10 torr	Different pulse time was tried, and optimum parameter was achieved	[77]
Triethyl borane and ammonia (V/III ratio varied between 2000 and 4000)	Sapphire substrate	Carrier gas flow rate was varied (H <sub>2</sub> )	Buffer layer at ≈600–800 Main epilayer ≥ 1400	Not mentioned	380 arcsec FWHM with excellent stoichiometric ratio and surface morphology	[77–82]
Same precursor was used with a varied NH <sub>3</sub> injection rate	Sapphire substrate	H <sub>2</sub> ; 27 slm	1000	3.85 kPa	Effect of NH <sub>3</sub> injection rate was observed and optimized	[78]

## 2.2. h-BN Device Fabrication Processes

To formulate the MSM detector device structures, freestanding h-BN layers are needed. Freestanding device layers can be obtained by the mechanical exfoliation process [79,80]. After the exfoliation process, films are diced into desired dimensions. Figure 4 shows the schematic of vertical and lateral devices. Metal contacts are formed as anode and cathode using a metallization process using e-beam evaporation. Different bilayer metal contacts have been deployed to measure device performance. Table 5 shows some of the physical parameters of devices. In the traditional room temperature semiconductor-based radiation

detector material CdZnTe, a different type of device and electrode geometry has been implemented. In the case of h-BN, most of the works are based on planar MSM geometry.

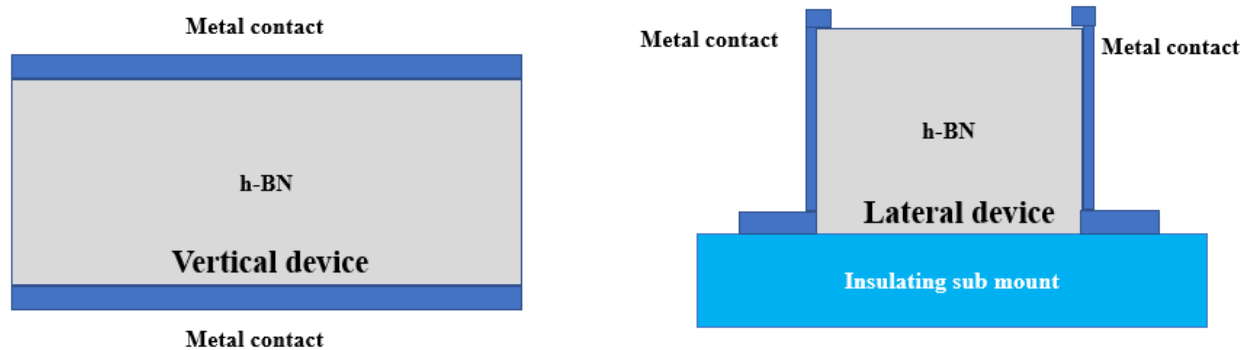


Figure 4. Cross-sectional schematic of lateral and vertical MSM neutron detector [74,82].

Table 5. Device physical parameters.

No.	Material Thickness	Contact Type	Device Type	Area of the Device	Ref.
1	0.3 $\mu\text{m}$	Ti/Al	Lateral	4.8 $\text{mm}^2$	[18]
2	0.3 $\mu\text{m}$	Ti/Al	Lateral	12 $\text{mm}^2$	[83]
3	0.3–43	Ti/Al	vertical	Not mentioned	[82]
4	43 $\mu\text{m}$	Ni/Au	vertical	1 $\text{mm}^2$	[79]
5	2.5–15 $\mu\text{m}$	Ti/Ti	vertical	40 $\text{mm}^2$ –14 $\text{mm}^2$	[81]
6	50 $\mu\text{m}$	Ni/Au	Vertical	9 $\text{mm}^2$	[80]
7	50 $\mu\text{m}$	Ni/Au and Ti/Al	vertical	1 $\text{mm}^2$	[76]
8	90 $\mu\text{m}$	Ni/Au	Lateral	29 $\text{mm}^2$	[84]
9	100 $\mu\text{m}$	Ni/Au	Lateral	1 $\text{cm}^2$	[85]

### 2.2.1. Etching

The etching of the h-BN requires external energy as an enabling agent to initiate and sustain the removal of surface atoms. The external energy can be in the form of ion bombardment in reactive ion etching (RIE). The bombardment of surfaces with ions can cause damage. RIE/selective RIE, with an emphasis on low damaged processes, has been investigated. Inductively coupled plasma reactive ion etching (ICP-RIE) using various gas mixtures of  $\text{BCl}_3/\text{SF}_6/\text{O}_2$  at low plasma-induced voltages (<60 V) has been employed by different groups [18,77–81].

### 2.2.2. Ohmic Contacts

There are limited works regarding ohmic contact formation on h-BN MSMs [77–81]. The reports start with Ti/Al metallization. Annealing Ti/Al without any overlayer, even in a full nitrogen environment, still produces a lot of surface oxides, which degrades contact resistance and makes the probe contacts nearly impossible. This has necessitated studies on Ti/Al-h-BN-Ti/Al, Ti/Al-h-BN-Ni/Au, Ni/Au-h-BN-Ti/Al, Ni/Au-h-BN-Ni/Au, and Ti/Ti-h-BN-Ti/Ti based contacts. Essential attributes of ohmic contact formation are low contact resistance, high edge acuity, low surface roughness, minimal lateral diffusion, and thermal stability. Doan et al. reported that Ni/Au-h-BN-Ni/Au is the best suitable contact material for h-BN based detectors with the highest efficiency [18,31,79–83].

In order to reduce the Ohmic contact area and check the efficiency variation, lateral devices have been deployed. The reported lateral devices use Ni/Au bilayer metal contacts varying the anode to cathode distance.

### 2.3. Experimental Setup

A high-density polyethylene (HDPE) moderator is usually used for the neutron measurement experimental setup purpose with a Californium–252 ( $^{252}\text{Cf}$ ) neutron source. The moderator is used to contain radioactive material as well as to convert fast neutrons to thermal neutrons. There are two holes, A and B, where hole A housed the source when in use and hole B housed the source when the measurement was completed. Hole B is much closer to the detector to increase the thermal neutron flux. The fabricated h-BN detector is usually placed at a certain distance away from the neutron source and covered with Al foil to reduce electronic noise. Readout electronics are used to quantify the signal from the detector [18,79]. A schematic of the experimental setup is shown in Figure 5.

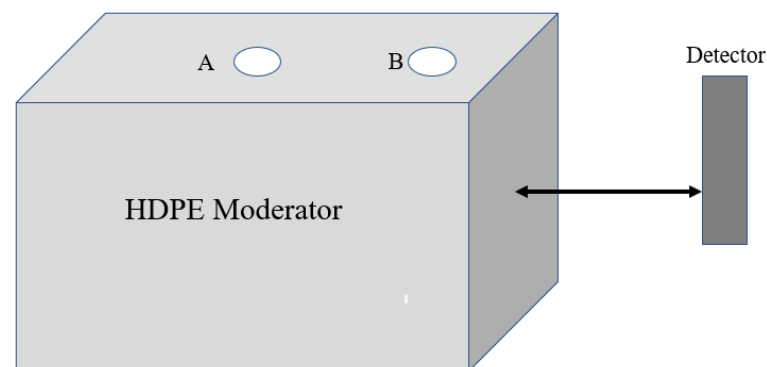


**Figure 5.** Experimental setup schematic for neutron absorption measurement [18,79].

There are several ways of building readout electronics [86,87]. The basic circuitry consists of a body of h-BN with two electrodes connected, which are described as the anode and cathode. The electrodes need to be perpendicular to the crystallographic axis of the h-BN. A high electric field needs to be applied parallel to the crystallographic axis of h-BN. The neutron flux is exposed to the device from a certain distance, and the produced current pulse is measured. To measure the signal, a charge sensitive amplifier, a pulse shaping amplifier is being connected to a multichannel analyzer (MCA), as shown in the schematic in Figure 6.

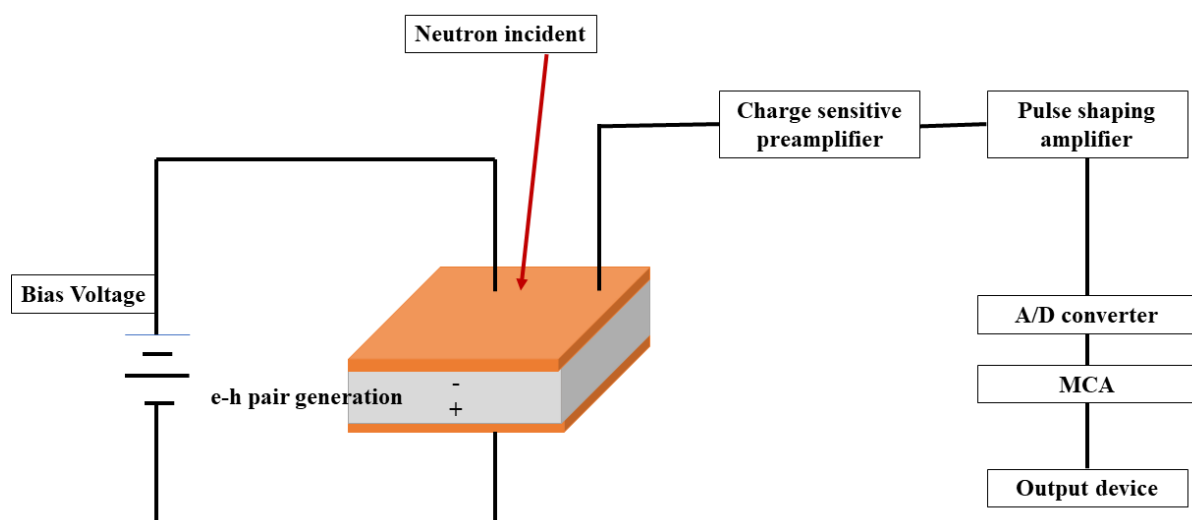


**Figure 6.** Schematic for the readout electronics [83,87].

### 3. Results and Discussions

#### 3.1. Point Defect Issues

The h-BN growth temperature is very high. So, oxygen and carbon impurities can occupy nitrogen sites denoted as  $O_N$  and  $C_N$ , respectively (subscript N means nitrogen atom). As shown in Figure 1, h-BN has a weak van der Waals force between its layers. So, it tends to peel off automatically or due to mechanical force from its substrate. It has been reported that  $O_N$  and  $C_N$  impurities are more common near the interface of h-BN and sapphire substrate (bottom surface) compared to the top surface of h-BN. It is important to choose which side of the grown device needs to be exposed to neutron absorption. Figure 7 shows a schematic of two different cases in vertical detectors. In case a (Figure 7a), a neutron is incoming through the top surface. After the incidence, the neutron flux decays based on the exponential decay formula ( $I = I_0 e^{(-\frac{x}{\lambda})}$ ), where  $I_0$  is the incident flux, and  $x$  is the distance from the incident surface). In case b (Figure 7b), the device is made such that neutrons are coming through the bottom surface. It shows that the choice of incidence orientation has an impact on neutron absorption. The top surface as a neutron incident interface is favorable as it has less  $O_N$ . Biasing voltage polarity is another important parameter to consider. In vertical devices, positive on the top surface or vice versa is implemented and tested. Du et al. showed that changing the carrier gas to more passive nitrogen gas can decrease oxygen and carbon occupancy in nitrogen sites [88,89].

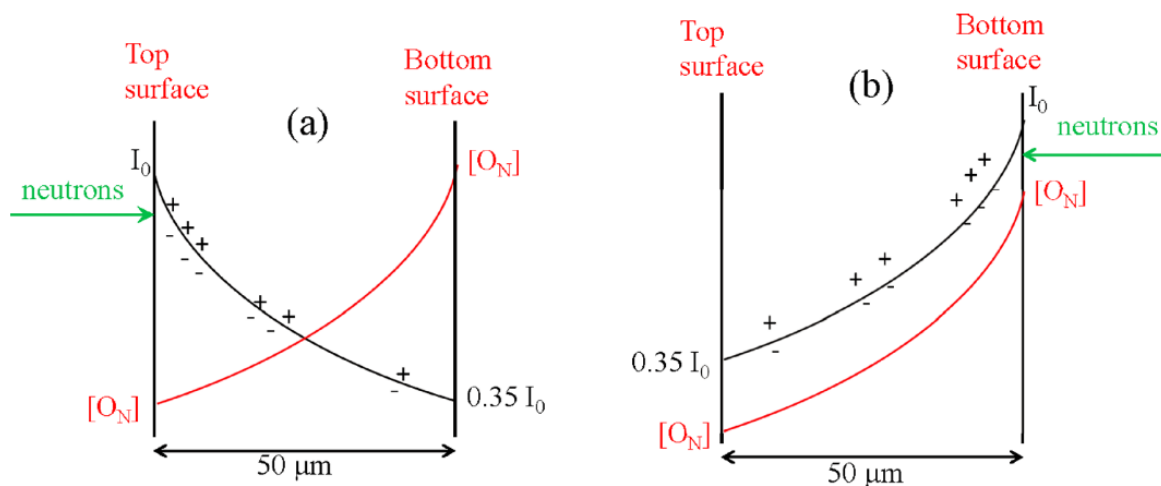


**Figure 7.** Schematic of oxygen occupancy in nitrogen sites with neutron incidence direction (a) from top surface, (b) from bottom surface [The figure is reproduced from [76] copyright 2018 with permission from AIP Publishing].

#### 3.2. Ohmic Contacts

Ohmic contact formation is another essential aspect to consider. The performance of the device largely depends on charge collection efficiency. The derived signal is amplified, integrated, and finally digitized to characterize using MCA. The presence of any kind of noise reduces the chance of detecting the original signal. The most common type of noise is ‘shot noise’, which largely depends on the leakage current of the device [90]. Different types of ohmic contacts have been researched, as mentioned in Table 5. In the case of vertical devices, Ni/Au has been tested as the best one with the highest efficiency and low leakage current. Most of the other works also follow the same Ni/Au-based ohmic contacts.

#### 3.3. Epilayer Thickness and Absorption Length

Diffusion lengths for Li and alpha particles are between 2 and 5  $\mu\text{m}$ . So, if the material thickness is more than the diffusion length, the Li and alpha particles are confined inside the detector material. Neutron absorption follows the below formula,

$$n_{abs} = \Phi_1 A (1 - e^{-d/\chi}) t \quad (3)$$

where  $t$  is the total counting time,  $d$  is the thickness of the h-BN epilayer,  $A$  is the cross-sectional area,  $n_{abs}$  is the neutron count,  $\Phi_1$  is the neutron flux, and  $\chi$  is the thermal neutron absorption length. Thus, the thickness of the material is a critical parameter. The material thickness needs to be higher than the neutron absorption length. Thickness-dependent data are shown in Figure 8 [31]. This was reported by Li et al., and the experiments were conducted at the Kansas State University TRIGA Mark II Reactor.

The boron density in h-BN is  $5 \times 10^{22} \text{ cm}^{-3}$  where 20% is  $^{10}\text{B}$ , and 80% is  $^{11}\text{B}$ . So, the density of  $^{10}\text{B}$  is around  $n = 1.1 \times 10^{22} \text{ cm}^{-3}$ . The neutron absorption coefficient,  $\alpha_{\text{natural}} = N\sigma = 42.24 \text{ cm}^{-1}$  and absorption length,  $\chi_{\text{natural}} = 1/\alpha_{\text{natural}} = 237 \text{ }\mu\text{m}$  where  $n = 1.1 \times 10^{22} \text{ cm}^{-3}$  and  $\sigma = 3840$  barns is the cross-section for  $^{10}\text{B}$  for thermal neutron (25.3 meV) [18]. If we can increase the amount of  $^{10}\text{B}$  percentage in h-BN, then the absorption length will decrease. In the case of 100%  $^{10}\text{B}$  enriched h-BN, the absorption length reduces to  $47.3 \text{ }\mu\text{m}$  [79]. Li et al. showed interesting experimental data in their paper, which shows the relationship between h-BN layer thickness and relative neutron transmission (Figure 8). They measured that the neutron absorption length for natural h-BN is around  $277 \text{ }\mu\text{m}$ , which is close to the theoretical value of  $237 \text{ }\mu\text{m}$  [31]. The electron–hole (e–h) pair generation energy is approximately three times the bandgap [36]. Thus, as per Equations (1) and (2), the neutron absorption process creates an average of 2.34 MeV energy, which corresponds to  $1.3 \times 10^5$  electron–hole (e–h) pairs generation [31].

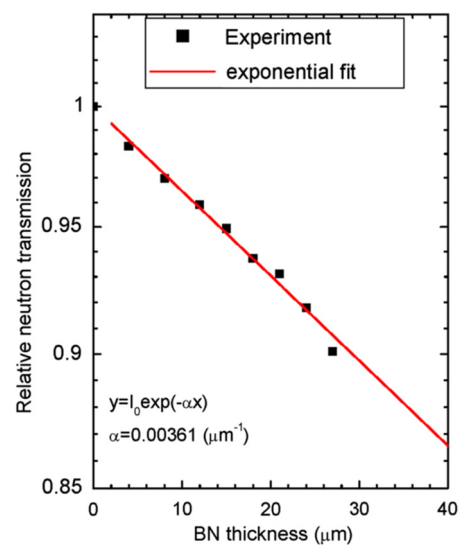


**Figure 8.** Neutron transmission dependency on h-BN epilayer thickness (the image is reproduced from [31], copyright 2011, with permission from Elsevier).

### 3.4. Mobility Lifetime Product

The absorbed neutrons create electron–hole (e–h) pairs in the semiconductor materials, which produce a detectable signal. It is essential to collect the e–h pairs generated before recombination. For this, the carrier transit time ( $\tau_t$ ) must be smaller than the e–h pair recombination time ( $\tau$ ) [18]. The relationship is as below:

$$\tau_t = \frac{L}{\mu E} = \frac{L^2}{\mu V} \quad (4)$$

where  $V$  is the applied bias voltage,  $E$  is the electric field, and  $L$  is the distance between electrodes. Most of the electrons can be collected if the below relation holds considering  $\tau_t < \tau$ ,

$$\tau\mu > \frac{L^2}{V} = \frac{LA}{\rho I} \quad (5)$$

where  $\rho$  is the resistivity of the material,  $I$  is the generated current in the external circuit, and  $A$  is the cross-sectional area. The mobility lifetime product thus depends on the device geometry, material quality, and as well as material resistivity. If the quality of the material is better, so is the resistivity; then, the mobility lifetime product becomes much higher. Doan et al. showed some of the measured results for their fabricated device. They showed that under a certain value, the neutron detection capability degrades [18]. Figure 9a shows their derived results for certain device geometry.

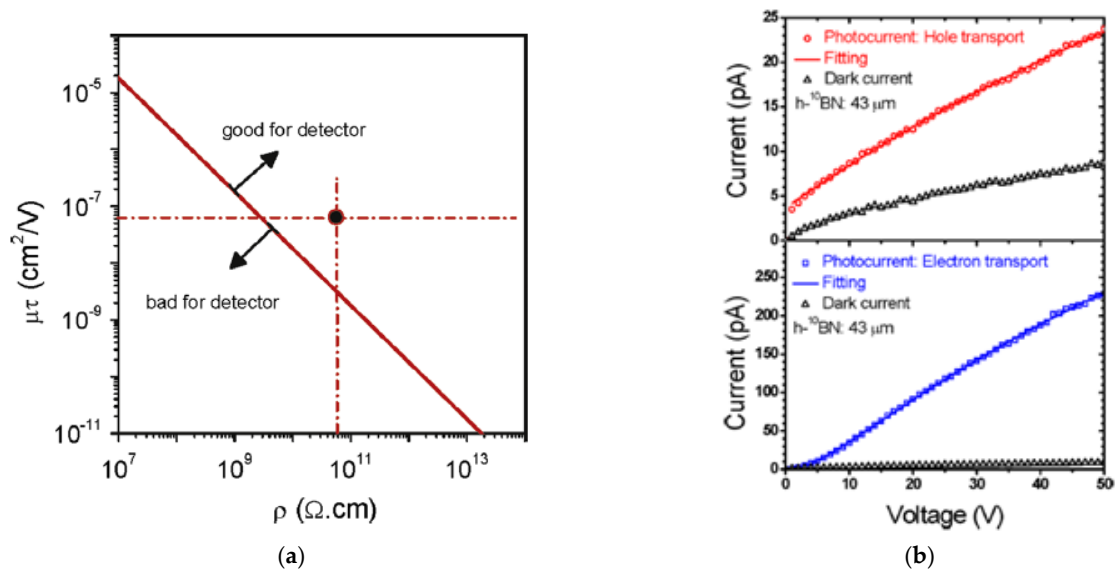


**Figure 9.** (a) Mobility lifetime product versus resistivity, (b) fitting of Many's equation to obtain product (Figure (a) is reproduced from [18] copyright 2014, with permission from Elsevier, and Figure (b) is reproduced from [79] copyright 2016 with permission from AIP publishing).

Now, the question arises of how to measure this mobility lifetime product of the fabricated device. All the published paper in this field follows Many's equation to calculate this parameter from the photocurrent characteristics under illumination curve fitting (as an example in Figure 9b) [91]:

$$I_i(V) = I_{0,i}\eta_{c,i} = I_{0,i}\left(\frac{\mu_i\tau_i V(1 - e^{-\frac{L^2}{\mu_i\tau_i V}})}{L^2(1 + \frac{S_i L}{\mu_i V})}\right), i = e, h \quad (6)$$

where  $\eta_c$  is the charge collection efficiency,  $I_0$  is the saturation current,  $i = e$  denotes the parameters for electrons,  $i = h$  denotes the parameters for holes,  $S_i$  is the surface recombination velocity, where  $E_s = S_i/\mu$  ( $\mu$  is the mobility and  $E_s$  is the applied electric field),  $V_b = V$  is the bias voltage applied between electrodes to accelerate charge carriers, which leads to an applied electric field as  $E_a = V/L$  where  $L$  is the distance between electrodes. Many's equation implies that to obtain better charge collection efficiency, (a) the carrier drift length needs to be larger than the transit distance, which is the same as in Equation (6), and (b) the external applied field needs to be larger than the surface recombination field to collect the charges from the detector [92]. From Doan et al., the better the h-BN quality, the higher the resistivity, and the higher the product, the higher the detector efficiency and sensitivity [18,82,83]. Maity et al. have reported that the  $\tau_i\mu_i$  product is much higher for holes compared to electrons, which contradicts some other reports [79]. Cao et al. have reported that the electron and hole effective mass in an h-BN single sheet is

the same as their mobility [93]; thus, a higher  $\tau_i\mu_i$  for holes means  $\tau_h \gg \tau_i$ . This is also one of the proofs that the undoped h-BN's quasi-Fermi level is below the intrinsic Fermi level, which means the material is naturally p-type [18,83]. Maity et al. showed in their report that considering the hole transport characteristics and device size, the resistivity of 43, 50, and 100  $\mu\text{m}$  thick h-BN film is  $\approx 10^{13}$  ohm-cm [76,80,84,85].

### 3.5. Pulse Height Spectra and Energy Resolution

With a certain applied electric field, all the charge carriers are collected via electrodes. This signal is then pre-amplified, passed through a Gaussian-shaped amplifier, and read via MCA [12,18,94]. The channel number vs. count data from MCA are resolved by fitting the data against the energy product vs. channel number, as shown in Figure 10 [83]. It has been reported that the data become more resolved if the material quality is much better with fewer charge carrier traps, fewer defects, higher  $\tau\mu$  products, and obviously, the material thickness needs to be much higher than the absorption length of Li and alpha particles (2–5  $\mu\text{m}$ ). The charge carrier trap issue is severe in polycrystalline materials. Doan et al. mentioned that the FWHM of Li and alpha particle peaks in MCA in the case of MSM h-BN detectors is less compared to boron-coated semiconductor detectors [18]. The energy resolution of h-BN based detectors has been reported to be much better compared to  $^{10}\text{B}$  perforated Si pillar-based indirect conversion detectors, as the Li and alpha particle absorption lengths are random due to charge carrier traps [16,95].

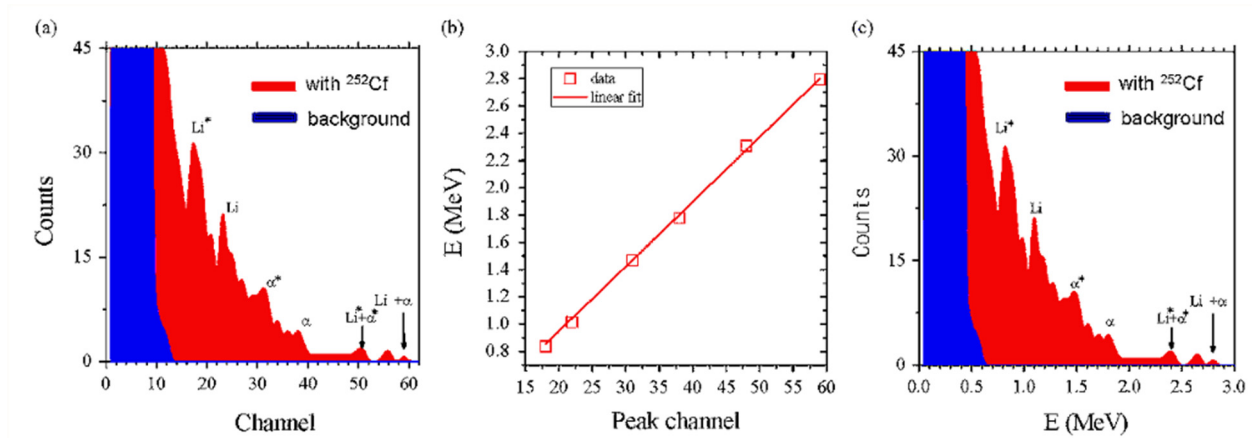


**Figure 10.** (a) Counts versus channel number, (b) energy peak calibration among all expected nuclear reaction products, and (c) counts vs. energy (MeV) (the figures are reproduced from [83] copyright 2013, with permission from Elsevier).

In Figure 10a,c, the blue column bars are the measured counts in the absence of the  $^{252}\text{Cf}$ (source), which is just the background noise. Figure 10b shows the linear relationship between the corresponding energy and MCA channel number. The red column bars are the measured counts in the presence of the  $^{252}\text{Cf}$ (source). As mentioned in Equations (1) and (2), the peak positions in Figure 10c show the energy corresponding to Li,  $\text{Li}^*$ ,  $\alpha$ , and  $\alpha^*$  peaks, as well as the sum peaks  $\text{Li} + \alpha$  and  $\text{Li}^* + \alpha^*$ .

### 3.6. Device Efficiency

Charge collection efficiency (CCE) is a very important parameter. It can be defined as  $\text{CCE} = \eta_{\text{coll}} = \frac{\eta}{P} = \frac{N_c/N_{\text{in}}}{t/\chi}$  where  $N_c$  is the measured neutron counts,  $N_{\text{in}}$  is the total neutron counts,  $t$  is the thickness of the sample,  $\chi$  is the thermal neutron absorption length, and  $P$  is the probability of interaction. It has been previously described that  $\chi = 237$   $\mu\text{m}$ . So, such a thicker defect-free single-crystal h-BN has not been reported yet. That is why the interaction probability cannot reach 100%. So far, the maximum thickness has been reported as 100  $\mu\text{m}$ ; in that case,  $P$  is around 37.8% [94].

h-BN detectors in the reports are calibrated against a commercially purchased neutron detector. Maity et al. reported a comparison with a  ${}^6\text{LiF}$  neutron detector with 33% efficiency. The neutrons count rate per unit area for h-BN and commercially purchased detectors are 77.2 and 45.1 n/s-cm<sup>2</sup>. Using the detection ratio, the authors calculated the efficiency of the h-BN detector as 51.4%. The Charge Collection Efficiency (CCE) at a bias voltage of 400 V was about 86.1%. The other parameters affecting the efficiency and sensitivity of the detector are the limitation of detector area and radioactive material to detector distance [79]. All the results so far have been derived and are based on natural  ${}^{10}\text{B}$  in h-BN. It has been proposed to use enriched  ${}^{10}\text{B}$  to increase the amount of neutron absorbing cross-section in the semiconductor material. In the case of vertical devices, the highest device area was achieved by Maity et al. as 90 mm<sup>2</sup> with 90  $\mu\text{m}$  epilayer thickness and 50% efficiency [84]. Previously, it has been reported by Maity et al. with 58% efficiency with 50  $\mu\text{m}$  thickness, but the device area is very small (1 mm<sup>2</sup>) [76].

### 3.7. Lateral vs. Vertical Devices

Scaling up the neutron detector is very important from the commercialized application point of view. The problem with vertical devices is if the device area is scaled up, then the efficiency and CCE increase, but the leakage current increases. Due to the increase in the ohmic contact area, the capacitance and surface recombination increase, ultimately lowering the CCE and efficiency [92]. The opposite has been demonstrated in the lateral device with a 29 mm<sup>2</sup> device size with 50% efficiency. In this report, the mobility lifetime product is higher compared to previously reported data. The in-plane mobility has been reported as 100 s more than the vertical mobility, which leads to higher CCE [92]. Resistivity is lower in the case of lateral devices, but due to less contact area, the surface recombination is less. So, the leakage current and the CCE are higher. As the contact area is significantly reduced in the case of lateral devices, the capacitance and RC time constant are also reduced. Surface trap states are reduced in the case of lateral devices due to less contact area. All these effects eventually lead to a high-efficiency detector with a higher surface area.

The most recent report regarding lateral device geometry is a 1 cm<sup>2</sup> device with 59% detection efficiency. The device thickness is 100  $\mu\text{m}$ . The significant improvement of material thickness and quality has resulted in a 6 s increase in the mobility lifetime product and 3 s decrease in the surface recombination field [85]. It is so far the best device data that have been demonstrated.

Table 6 summarizes the results of the recent works based on their different properties.

**Table 6.** Summary of the results found in different references.

No.	Material Thickness in $\mu\text{m}$	$\tau\mu$ for Electrons	$\tau\mu$ for Holes	Resistivity	Material Specimen in mCi (Millicurie)	Area of the Device in mm <sup>2</sup>	Bias Voltage in V	Time Measured	Efficiency	Reference
1	0.3	$4.5 \times 10^{-8}$	$7.1 \times 10^{-9}$	$5.3 \times 10^{10}$	2.4	4.8	240	26 h	Not mentioned	[18]
2	50	$1.0 \times 10^{-6}$	$1.0 \times 10^{-6}$	Not mentioned	Not mentioned	1	200	Not mentioned	58%	[76]
3	43	$8.3 \times 10^{-7}$	$2.2 \times 10^{-5}$	$1.0 \times 10^{13}$	0.93	1	400	10 min	51.40%	[79]
4	50	$2.0 \times 10^{-6}$	$1.0 \times 10^{-5}$	$1.0 \times 10^{13}$	0.77	9	200	15 min	53%	[80]
5	2.5–15	$3.0 \times 10^{-7}$	$5.0 \times 10^{-8}$	$3.0 \times 10^9$	Not mentioned	14–40	700, 450, 600, 700	Not mentioned	4.21–21.37%	[81]
6	0.3–43	$3.3 \times 10^{-7}$	$3.3 \times 10^{-7}$	$5.0 \times 10^{10}$	Not mentioned	Not mentioned	Variable	20 min	51.40% (43 $\mu\text{m}$ )	[82]
7	0.3	$2.83 \times 10^{-7}$	$2.83 \times 10^{-7}$	$5.0 \times 10^{10}$	1.6	12	20	Not mentioned	Not mentioned	[83]
8	90	$1.0 \times 10^{-4}$	$1.0 \times 10^{-4}$	Not mentioned	0.5	29	400	15 min	50%	[84]
9	100	$5.0 \times 10^{-3}$	$5.0 \times 10^{-3}$	$1.0 \times 10^{12}$	0.45	100	500	15 min	59%	[85]

#### 4. Conclusions

MSM detectors based on h-BN have been mainly being researched for the last ten years, and still, it is a premature technology. The challenge regarding fewer defects and thicker material growth has been addressed. Still, the oxygen occupancy issue needs to be solved. In all the previous works, the MOCVD growth of h-BN is on sapphire. As h-BN growth is a high-temperature process, oxygen occupancy near the substrate has not been solved. One solution can be to grow some other type of template material such as AlN and then grow h-BN on top of the AlN buffer layer. In that case, the oxygen vacancy issue can be addressed. This hypothesis has not been tested yet. The neutron absorption length for h-BN is 237  $\mu\text{m}$ . So far, material up to 100  $\mu\text{m}$  has been grown, and the detector is being fabricated to obtain high efficiency. More than 100  $\mu\text{m}$  thickness has not been reported yet. Although vertical and lateral types have been reported, the maximum efficiency has been reported for lateral devices with 59% and 1  $\text{cm}^2$  device area. Vertical devices have also shown good neutron detection efficiency (58%) and CCE (86%) but suffer from low device area, leading to less neutron flux absorption. Vertical devices have shown lower mobility as well as a lower mobility lifetime product, higher surface recombination field due to higher surface traps, higher capacitance due to the higher contact area, and, as mentioned before, less neutron flux. All these parameters reduce device sensitivity. It has been shown that the lateral device is a better option to increase the device area, but there is a tradeoff between efficiency and area. In the case of the lateral device, the mobility lifetime product has been increased, while the leakage current, capacitance, and surface recombination effect have been decreased. Not that much work has been done regarding the metal contacts. More attention is required in this field to reduce the leakage current. This might have an implication on the overall device performance. h-BN-based neutron detectors can be very promising, but the commercial implementation still needs lots of R&D based work in the coming days to be used in real-life application.

**Supplementary Materials:** The following supporting information can be downloaded at: <https://www.mdpi.com/article/10.3390/electronicmat3030020/s1>, Figure S1: Schematic of a CVD set up for the epitaxy of h-BN.

**Author Contributions:** Conceptualization, methodology, visualization, investigation, writing of original draft: S.H.; Editing, revision, supervision and PI of the study: I.A. All authors have read and agreed to the published version of the manuscript.

**Funding:** This work was supported by the National Science Foundation (NSF) award No. 2124624 managed by Dominique M. Dagenais and SCEE research initiation grant for 2021–2022.

**Data Availability Statement:** Data is available in the mentioned references and upon reasonable request.

**Acknowledgments:** The authors thank Didarul Alam, Doctoral Student, Electrical Engineering Department, University of South Carolina for his valuable input.

**Conflicts of Interest:** The authors declare that they have no conflict of interest.

#### References

1. U.S. Department of Energy (DOE). *DOE Fundamentals Handbook Nuclear Physics Volume 2 of 2*; U.S. Department of Energy: Washington, DC, USA, 1993; Volume 1, p. 36.
2. McGregor, D.S.; Klann, R.T.; Gersch, H.K.; Yang, Y.H. Thin-film-coated bulk GaAs detectors for thermal and fast neutron measurements. *Nucl. Instrum. Methods Phys. Res. Sect. A Accel. Spectrom. Detect. Assoc. Equip.* **2001**, *466*, 126–141. [[CrossRef](#)]
3. Coleman, R. The Application of Neutron Activation Analysis to Forensic Science. *J. Forensic Sci. Soc.* **1967**, *6*, 19–22. [[CrossRef](#)]
4. Youmans, A.H. Conduction Counter for Radioactivity Well Logging. U.S. Patent 2,760,078, 21 August 1956.
5. Yazbeck, J. Investigations of Hexagonal Boron Nitride as a Semiconductor for Neutron Detection. Ph.D. Thesis, Kansas State University, Manhattan, NY, USA, August 2012.
6. Caruso, A.N. The Physics of Solid-State Neutron Detector Materials and Geometries. *J. Phys. Condens. Matter* **2010**, *22*, 443201. [[CrossRef](#)] [[PubMed](#)]
7. Beckurts, K.H.; Wirtz, K. *Neutron Physics*; Springer Science & Business Media: Berlin/Heidelberg, Germany, 29 June 2013.

8. Knoll, G.F. *Radiation Detection and Measurement*, 3rd ed.; John Wiley and Sons Inc.: New York, NY, USA, 2009; pp. 1–796.
9. Kouzes, R.T.; Ely, J.H.; Erikson, L.E.; Kernan, W.J.; Lintereur, A.T.; Siciliano, E.R.; Stephens, D.L.; Stromswold, D.C.; Van Ginhoven, R.M.; Woodring, M.L. Neutron Detection Alternatives to  $^3\text{He}$  for National Security Applications. *Nucl. Instrum. Methods Phys. Res. Sect. A Accel. Spectrom. Detect. Assoc. Equip.* **2010**, *623*, 1035–1045. [[CrossRef](#)]
10. Angelone, M. *Neutron Detection: Principles, Methods, Issues (and Tips)* Maurizio Angelone; ENEA Frascati: Rome, Italy, 2009.
11. McGregor, D.S.; Shultis, J.K. Spectral identification of thin-film-coated and solid-form semiconductor neutron detectors. *Nucl. Instrum. Methods Phys. Res. Sect. A Accel. Spectrom. Detect. Assoc. Equip.* **2004**, *517*, 180–188. [[CrossRef](#)]
12. Nikolic, R.J.; Cheung, C.L.; Reinhardt, C.E.; Wang, T.F. Roadmap for High Efficiency Solid-State Neutron Detectors. In Proceedings of the Optoelectronic Devices: Physics, Fabrication, and Application II, Boston, MA, USA, 23–26 October 2005; Volume 15, p. 601305. [[CrossRef](#)]
13. Nikolic, R.J.; Conway, A.M.; Reinhardt, C.E.; Graff, R.T.; Wang, T.F.; Deo, N.; Cheung, C.L. Pillar structured thermal neutron detector with 6:1 aspect ratio. *Appl. Phys. Lett.* **2008**, *93*, 133502. [[CrossRef](#)]
14. Bellinger, S.L.; Fronk, R.G.; McNeil, W.J.; Sobering, T.J.; McGregor, D.S. Enhanced variant designs and characteristics of the microstructured solid-state neutron detector. *Nucl. Instrum. Methods Phys. Res. Sect. A Accel. Spectrom. Detect. Assoc. Equip.* **2011**, *652*, 387–391. [[CrossRef](#)]
15. Clinton, J. Optimization and Characterization of a Novel Self Powered Solid State Neutron Detector. Ph.D. Thesis, Rensselaer Polytechnic Institute, Troy, NY, USA, December 2011.
16. Shao, Q.; Voss, L.F.; Conway, A.M.; Nikolic, R.J.; Dar, M.A.; Cheung, C.L. High Aspect Ratio Composite Structures with 48.5% Thermal Neutron Detection Efficiency. *Appl. Phys. Lett.* **2013**, *102*, 063505. [[CrossRef](#)]
17. Osberg, K.; Schemm, N.; Balkir, S.; Brand, J.I.; Hallbeck, M.S.; Dowben, P.A.; Hoffman, M.W. A handheld neutron-detection sensor system utilizing a new class of boron carbide diode. *IEEE Sens. J.* **2006**, *6*, 1531–1538. [[CrossRef](#)]
18. Doan, T.C.; Majety, S.; Grenadier, S.; Li, J.; Lin, J.Y.; Jiang, H.X. Fabrication and Characterization of Solid-State Thermal Neutron Detectors Based on Hexagonal Boron Nitride Epilayers. *Nucl. Instrum. Methods Phys. Res. Sect. A Accel. Spectrom. Detect. Assoc. Equip.* **2014**, *748*, 84–90. [[CrossRef](#)]
19. Jiang, H.X.; Lin, J.Y. Hexagonal boron nitride epilayers: Growth, optical properties and device applications. *ECS J. Solid State Sci. Technol.* **2016**, *6*, Q3012. [[CrossRef](#)]
20. Huang, K.C.; Dahal, R.; Lu, J.J.Q.; Weltz, A.; Danon, Y.; Bhat, I.B. Scalable Large-Area Solid-State Neutron Detector with Continuous p-n Junction and Extremely Low Leakage Current. *Nucl. Instrum. Methods Phys. Res. Sect. A Accel. Spectrom. Detect. Assoc. Equip.* **2014**, *763*, 260–265. [[CrossRef](#)]
21. Shultis, J.K.; McGregor, D.S. Design and performance considerations for perforated semiconductor thermal-neutron detectors. *Nucl. Instrum. Methods Phys. Res. Sect. A Accel. Spectrom. Detect. Assoc. Equip.* **2009**, *606*, 608–636. [[CrossRef](#)]
22. Alam, M.D.; Nasim, S.S.; Hasan, S. Recent progress in CdZnTe based room temperature detectors for nuclear radiation monitoring. *Prog. Nucl. Energy* **2021**, *140*, 103918. [[CrossRef](#)]
23. McGregor, D.S.; Hammig, M.D.; Yang, Y.H.; Gersch, H.K.; Klann, R.T. Design considerations for thin film coated semiconductor thermal neutron detectors—I: Basics regarding alpha particle emitting neutron reactive films. *Nucl. Instrum. Methods Phys. Res. Sect. A Accel. Spectrom. Detect. Assoc. Equip.* **2003**, *500*, 272–308. [[CrossRef](#)]
24. Gersch, H.K.; McGregor, D.S.; Simpson, P.A. The effect of incremental gamma-ray doses and incremental neutron fluences upon the performance of self-biased 10B-coated high-purity epitaxial GaAs thermal neutron detectors. *Nucl. Instrum. Methods Phys. Res. Sect. A Accel. Spectrom. Detect. Assoc. Equip.* **2002**, *489*, 85–98. [[CrossRef](#)]
25. Dahal, R.; Huang, K.C.; Clinton, J.; Licausi, N.; Lu, J.Q.; Danon, Y.; Bhat, I. Self-Powered Micro-Structured Solid State Neutron Detector with Very Low Leakage Current and High Efficiency. *Appl. Phys. Lett.* **2012**, *100*, 243507. [[CrossRef](#)]
26. Nelson, R.O.; Vogel, S.C.; Hunter, J.F.; Watkins, E.B.; Losko, A.S.; Tremsin, A.S.; Borges, N.P.; Cutler, T.E.; Dickman, L.T.; Espy, M.A.; et al. Neutron imaging at LANSCE—From cold to ultrafast. *J. Imaging* **2018**, *4*, 45. [[CrossRef](#)]
27. Rose, A. Sputtered boron films on silicon surface barrier detectors. *Nucl. Instrum. Methods* **1967**, *52*, 166–170. [[CrossRef](#)]
28. Doty, P.F. Boron Nitride Solid State Neutron Detector. U.S. Patent 6,727,504, 27 April 2004.
29. Robinson, J. Novel Carborane Derived Semiconducting Thin Films for Neutron Detection and Device Applications. Doctoral Dissertation, University of North Texas, Denton, TX, USA, 2015.
30. McGregor, D.S.; Unruh, T.C.; McNeil, W.J. Thermal neutron detection with pyrolytic boron nitride. *Nucl. Instrum. Methods Phys. Res. Sect. A Accel. Spectrom. Detect. Assoc. Equip.* **2008**, *591*, 530–533. [[CrossRef](#)]
31. Li, J.; Dahal, R.; Majety, S.; Lin, J.Y.; Jiang, H.X. Hexagonal Boron Nitride Epitaxial Layers as Neutron Detector Materials. *Nucl. Instrum. Methods Phys. Res. Sect. A Accel. Spectrom. Detect. Assoc. Equip.* **2011**, *654*, 417–420. [[CrossRef](#)]
32. Jiang, H.; Lin, J.; Li, J.; Maity, A.; Grenadier, S. Solid-State Neutron Detector. U.S. Patent 20200135958A1, 14 July 2018.
33. Nava, F.; Bertuccio, G.; Cavallini, A.; Vittone, E. Silicon Carbide and Its Use as a Radiation. *Meas. Sci. Technol.* **2008**, *19*, 102001. [[CrossRef](#)]
34. Del Sordo, S.; Abbene, L.; Caroli, E.; Mancini, A.M.; Zappettini, A.; Ubertini, P. Progress in the Development of CdTe and CdZnTe Semiconductor Radiation Detectors for Astrophysical and Medical Applications. *Sensors* **2009**, *9*, 3491–3526. [[CrossRef](#)] [[PubMed](#)]
35. Laturia, A.; Van de Put, M.L.; Vandenberghe, W.G. Dielectric Properties of Hexagonal Boron Nitride and Transition Metal Dichalcogenides: From Monolayer to Bulk. *NPJ 2D Mater. Appl.* **2018**, *2*, 6. [[CrossRef](#)]

36. Klein, C.A. Bandgap dependence and related features of radiation ionization energies in semiconductors. *J. Appl. Phys.* **1968**, *39*, 2029–2038. [[CrossRef](#)]
37. Li, J.; Majety, S.; Dahal, R.; Zhao, W.P.; Lin, J.Y.; Jiang, H.X. Dielectric Strength, Optical Absorption, and Deep Ultraviolet Detectors of Hexagonal Boron Nitride Epilayers. *Appl. Phys. Lett.* **2012**, *101*, 171112. [[CrossRef](#)]
38. Majety, S.; Li, J.; Cao, X.K.; Dahal, R.; Lin, J.Y.; Jiang, H.X. Metal-Semiconductor-Metal Neutron Detectors Based on Hexagonal Boron Nitride Epitaxial Layers. In Proceedings of the Hard X-Ray, Gamma-Ray, and Neutron Detector Physics XIV, San Diego, CA, USA, 2–16 August 2012.
39. Grenadier, S.; Li, J.; Lin, J.; Jiang, H. Dry Etching Techniques for Active Devices Based on Hexagonal Boron Nitride Epilayers. *J. Vac. Sci. Technol. A Vac. Surf. Film.* **2013**, *31*, 61517. [[CrossRef](#)]
40. Majety, S.; Cao, X.K.; Dahal, R.; Pantha, B.N.; Li, J.; Lin, J.Y.; Jiang, H.X. Semiconducting Hexagonal Boron Nitride for Deep Ultraviolet Photonics. In Proceedings of the Quantum Sensing and Nanophotonic Devices IX, San Diego, CA, USA, 21–26 January 2012. [[CrossRef](#)]
41. Li, J.; Gui, G.; Zhong, J. Tunable Bandgap Structures of Two-Dimensional Boron Nitride. *J. Appl. Phys.* **2008**, *104*, 094311. [[CrossRef](#)]
42. Pacilé, D.; Meyer, J.C.; Girit, Ç.Ö.; Zettl, A. The two-dimensional phase of boron nitride: Few-atomic-layer sheets and suspended membranes. *Appl. Phys. Lett.* **2008**, *92*, 133107. [[CrossRef](#)]
43. Li, L.; Chen, Y.I.; Zhang, H.; Li, L.H.; Chen, Y.; Behan, G.; Petravic, M.; Glushenkov, A.M. Large-Scale Mechanical Peeling of Boron Nitride Nanosheets by Low-Energy Ball Milling Large-Scale Mechanical Peeling of Boron Nitride Nanosheets by Low-Energy Ball Milling. *Artic. J. Mater. Chem.* **2011**, *21*, 11862–11866. [[CrossRef](#)]
44. Coleman, J.N.; Lotya, M.; O’Neill, A.; Bergin, S.D.; King, P.J.; Khan, U.; Nicolosi, V. Two-dimensional nanosheets produced by liquid exfoliation of layered materials. *Science* **2011**, *331*, 568–571. [[CrossRef](#)]
45. Lin, Y.; Williams, T.V.; Connell, J.W. Soluble, exfoliated hexagonal boron nitride nanosheets. *J. Phys. Chem. Lett.* **2010**, *1*, 277–283. [[CrossRef](#)]
46. Han, W.Q.; Wu, L.; Zhu, Y.; Watanabe, K.; Taniguchi, T. Structure of Chemically Derived Mono- and Few-Atomic-Layer Boron Nitride Sheets. *Appl. Phys. Lett.* **2008**, *93*, 223103. [[CrossRef](#)]
47. Zhi, C.; Ueda, S.; Zeng, H.; Wang, X.; Tian, W.; Wang, X.; Bando, Y.; Golberg, D. Weak Morphology Dependent Valence Band Structure of Boron Nitride. *J. Appl. Phys.* **2013**, *114*, 054306. [[CrossRef](#)]
48. Jin, C.; Lin, F.; Suenaga, K.; Iijima, S. Fabrication of a Freestanding Boron Nitride Single Layer and Its Defect Assignments. *APS Phys.* **2009**, *102*, 195505. [[CrossRef](#)]
49. Warner, J.H.; Rummeli, M.H.; Bachmatiuk, A.; Büchner, B. Atomic Resolution Imaging and Topography of Boron Nitride Sheets Produced by Chemical Exfoliation. *ACS Nano* **2010**, *4*, 1299–1304. [[CrossRef](#)]
50. Meyer, J.C.; Chuvilin, A.; Algara-Siller, G.; Biskupek, J.; Kaiser, U. Selective Sputtering and Atomic Resolution Imaging of Atomically Thin Boron Nitride Membranes. *Nano Lett.* **2009**, *9*, 2683–2689. [[CrossRef](#)]
51. Li, X.; Hao, X.; Zhao, M.; Wu, Y.; Yang, J.; Tian, Y.; Qian, G. Exfoliation of Hexagonal Boron Nitride by Molten Hydroxides. *Adv. Mater.* **2013**, *25*, 2200–2204. [[CrossRef](#)]
52. Wang, X.; Zhi, C.; Li, L.; Zeng, H.; Li, C.; Mitome, M.; Golberg, D.; Bando, Y. “Chemical Blowing” of Thin-Walled Bubbles: High-Throughput Fabrication of Large-Area, Few-Layered BN and C x-BN Nanosheets. *Adv. Mater.* **2011**, *23*, 4072–4076. [[CrossRef](#)]
53. Wang, X.-B.; Weng, Q.; Wang, X.; Li, X.; Zhang, J.; Liu, F.; Jiang, X.F.; Guo, H.; Xu, N.; Golberg, D.; et al. Biomass-Directed Synthesis of 20 g High-Quality Boron Nitride Nanosheets for Thermoconductive Polymeric Composites. *ACS Nano* **2014**, *8*, 9081–9088. [[CrossRef](#)]
54. Nag, A.; Raidongia, K.; Hembram, K.P.S.S.; Datta, R.; Waghmare, U.V.; Rao, C.N.R. Graphene Analogues of BN: Novel Synthesis and Properties. *ACS Nano* **2010**, *4*, 1539–1544. [[CrossRef](#)]
55. Zhang, X.; Qin, J.; Xue, Y.; Yu, P.; Zhang, B.; Wang, L.; Liu, R. Effect of aspect ratio and surface defects on the photocatalytic activity of ZnO nanorods. *Sci. Rep.* **2014**, *4*, 4596. [[CrossRef](#)] [[PubMed](#)]
56. Gao, R.; Yin, L.; Wang, C.; Qi, Y.; Lun, N.; Zhang, L.; Liu, Y.X.; Kang, L.; Wang, X. High-Yield Synthesis of Boron Nitride Nanosheets with Strong Ultraviolet. *J. Phys. Chem. C* **2009**, *113*, 15160–15165. [[CrossRef](#)]
57. Hasan, S.; Mamun, A.; Hussain, K.; Gaevski, M.; Ahmad, I.; Khan, A. Growth Evolution of High-Quality MOCVD Aluminum Nitride Using Nitrogen as Carrier Gas on the Sapphire Substrate. *J. Mater. Res.* **2021**, *36*, 4360–4369. [[CrossRef](#)]
58. Hasan, S.; Mamun, A.; Hussain, K.; Patel, D.; Gaevski, M.; Ahmad, I.; Khan, A. Investigation of MOCVD Grown Crack-Free 4 Mm Thick Aluminum Nitride Using Nitrogen as a Carrier Gas. *MRS Adv.* **2021**, *6*, 456–460. [[CrossRef](#)]
59. Boo, J.H.; Rohr, C.; Ho, W. MOCVD of BN and GaN Thin Films on Silicon: New Attempt of GaN Growth with BN Buffer Layer. *J. Cryst. Growth* **1998**, *189*, 439–444. [[CrossRef](#)]
60. Coudurier, N.; Boichot, R.; Mercier, F.; Reboud, R.; Lay, S.; Blanquet, E.; Pons, M. Growth of boron nitride on (0001) AlN templates by High Temperature-Hydride Vapor Phase Epitaxy (HT-HVPE). *Phys. Procedia* **2013**, *46*, 102–106. [[CrossRef](#)]
61. Snure, M.; Paduano, Q.; Kiefer, A. Effect of Surface Nitridation on the Epitaxial Growth of Few-Layer Sp2BN. *J. Cryst. Growth* **2016**, *436*, 16–22. [[CrossRef](#)]
62. Wu, Q.; Yan, J.; Zhang, L.; Chen, X.; Wei, T.; Li, Y.; Liu, Z.; Wei, X.; Zhang, Y.; Wang, J.; et al. Growth Mechanism of AlN on Hexagonal BN/Sapphire Substrate by Metal-Organic Chemical Vapor Deposition. *CrystEngComm* **2017**, *19*, 5849–5856. [[CrossRef](#)]

63. Hasan, S.; Jewel, M.U.; Karakalos, S.G.; Gaevski, M.; Ahmad, I. Comparative Spectroscopic Study of Aluminum Nitride Grown by MOCVD in H<sub>2</sub> and N<sub>2</sub> Reaction Environment. *Coatings* **2022**, *12*, 924. [[CrossRef](#)]
64. Tay, R.Y. *Chemical Vapor Deposition Growth and Characterization of Two-Dimensional Hexagonal Boron Nitride*; Springer: Singapore, Singapore, 2018; ISBN 978-981-10-8808-7.
65. Nakamura, K.; Sasaki, T. Boron Nitride Films Prepared by MOCVD. *J. Solid State Chem.* **2000**, *154*, 101–106. [[CrossRef](#)]
66. Han, M.; Ryu, B.D.; Ko, K.B.; Jo, C.H.; Lim, C.-H.; Cuong, T.V.; Han, N.; Hong, C.H. Characteristics of Aluminum Nitride Films on Hexagonal Boron Nitride Buffer Layers Using Various Growth Methods through Metal Organic Chemical Vapor Deposition. *J. Cryst. Growth* **2019**, *507*, 316–320. [[CrossRef](#)]
67. Yang, F.H. *Modern Metal-Organic Chemical Vapor Deposition (MOCVD) Reactors and Growing Nitride-Based Materials*; Woodhead Publishing Limited: Cambridge, UK, 2013; ISBN 9780857095077.
68. Patriarche, G.; Ougazzaden, A.; Li, X.; Alam, S.; Sundaram, S.; Halfaya, Y. Wafer-Scale MOVPE Growth and Characterization of Highly Ordered h-BN on Patterned Sapphire Substrates. *J. Cryst. Growth* **2018**, *509*, 40–43. [[CrossRef](#)]
69. Lee, H.-J.; Honda, Y.; Amano, H.; Bae, S.-Y.; Yang, X.; Pristovsek, M.; Nagamatsu, K.; Liu, Y.; Nitta, S. Growth of Hexagonal Boron Nitride on Sapphire Substrate by Pulsed-Mode Metalorganic Vapor Phase Epitaxy. *J. Cryst. Growth* **2017**, *482*, 1–8. [[CrossRef](#)]
70. Eichler, J.; Lesniak, C. Boron nitride (BN) and BN composites for high-temperature applications. *J. Eur. Ceram. Soc.* **2008**, *28*, 1105–1109. [[CrossRef](#)]
71. Tingsuwatit, A.; Maity, A.; Grenadier, S.J.; Li, J.; Lin, J.Y.; Jiang, H.X. Boron nitride neutron detector with the ability for detecting both thermal and fast neutrons. *Appl. Phys. Lett.* **2022**, *120*, 232103. [[CrossRef](#)]
72. Caban, P.A.; Teklinska, D.; Michalowski, P.P.; Gaca, J.; Wojcik, M.; Grzonka, J.; Ciepiewski, P.; Mozdzonek, M.; Baranowski, J.M. The Role of Hydrogen in Carbon Incorporation and Surface Roughness of MOCVD-Grown Thin Boron Nitride. *J. Cryst. Growth* **2018**, *498*, 71–76. [[CrossRef](#)]
73. Halfaya, Y.; Sundaram, S.; Patriarche, G.; Li, X.; Alam, S.; Salvestrini, J.P.; Voss, P.L.; Ougazzaden, A.; Ayari, T. MOVPE van Der Waals Epitaxial Growth of AlGa<sub>N</sub>/AlGa<sub>N</sub> Multiple Quantum Well Structures with Deep UV Emission on Large Scale 2D h-BN Buffered Sapphire Substrates. *J. Cryst. Growth* **2018**, *507*, 352–356. [[CrossRef](#)]
74. Kobayashi, Y.; Akasaka, T. Hexagonal BN Epitaxial Growth on (0001) Sapphire Substrate by MOVPE. *J. Cryst. Growth* **2008**, *310*, 5044–5047. [[CrossRef](#)]
75. Jana, M.; Singh, R.N. Progress in CVD Synthesis of Layered Hexagonal Boron Nitride with Tunable Properties and Their Applications. *Int. Mater. Rev.* **2018**, *63*, 162–203. [[CrossRef](#)]
76. Maity, A.; Grenadier, S.J.; Li, J.; Lin, J.Y.; Jiang, H.X. Hexagonal Boron Nitride Neutron Detectors with High Detection Efficiencies. *J. Appl. Phys.* **2018**, *123*, 044501. [[CrossRef](#)]
77. Zheng, F.; Xiao, X.; Xie, J.; Zhou, L.; Li, Y.; Dong, H. Structures, properties and applications of two-dimensional metal nitrides: From nitride MXene to other metal nitrides. *2D Mater.* **2022**, *9*, 022001. [[CrossRef](#)]
78. Yang, X.; Nitta, S.; Pristovsek, M.; Liu, Y.; Nagamatsu, K.; Kushimoto, M.; Amano, H. Interface amorphization in hexagonal boron nitride films on sapphire substrate grown by metalorganic vapor phase epitaxy. *Appl. Phys. Express* **2018**, *11*, 051002. [[CrossRef](#)]
79. Maity, A.; Doan, T.C.; Li, J.; Lin, J.Y.; Jiang, H.X. Realization of Highly Efficient Hexagonal Boron Nitride Neutron Detectors. *Appl. Phys. Lett.* **2016**, *109*, 072101. [[CrossRef](#)]
80. Maity, A.; Grenadier, S.J.; Li, J.; Lin, J.Y.; Jiang, H.X. Toward Achieving Flexible and High Sensitivity Hexagonal Boron Nitride Neutron Detectors. *Appl. Phys. Lett.* **2017**, *111*, 033507. [[CrossRef](#)]
81. Ahmed, K.; Dahal, R.; Weltz, A.; Lu, J.J.Q.; Danon, Y.; Bhat, I.B. Solid-State Neutron Detectors Based on Thickness Scalable Hexagonal Boron Nitride. *Appl. Phys. Lett.* **2017**, *110*, 023503. [[CrossRef](#)]
82. Doan, T.C.; Marty, A.; Li, J.; Lin, J.Y.; Jiang, H.X. Thermal Neutron Detectors Based on Hexagonal Boron Nitride Epilayers. In Proceedings of the Hard X-Ray, Gamma-Ray, and Neutron Detector Physics XVIII, San Diego, CA, USA, 28 August–1 September 2016; Volume 9968, p. 99680S. [[CrossRef](#)]
83. Doan, T.C.; Majety, S.; Grenadier, S.; Li, J.; Lin, J.Y.; Jiang, H.X. Hexagonal Boron Nitride Thin Film Thermal Neutron Detectors with High Energy Resolution of the Reaction Products. *Nucl. Instrum. Methods Phys. Res. Sect. A Accel. Spectrom. Detect. Assoc. Equip.* **2015**, *783*, 121–127. [[CrossRef](#)]
84. Maity, A.; Grenadier, S.J.; Li, J.; Lin, J.Y.; Jiang, H.X. High Sensitivity Hexagonal Boron Nitride Lateral Neutron Detectors. *Appl. Phys. Lett.* **2019**, *114*, 222102. [[CrossRef](#)]
85. Maity, A.; Grenadier, S.J.; Li, J.; Lin, J.Y.; Jiang, H.X. High Efficiency Hexagonal Boron Nitride Neutron Detectors with 1 Cm<sup>2</sup> Detection Areas. *Appl. Phys. Lett.* **2020**, *116*, 142102. [[CrossRef](#)]
86. Dong, C.; Huang, Q.; Ma, X.; Yao, J.; Xiong, H.; Shen, F.; Chen, J.; Zhang, J.; Zhou, R. Readout electronics for thermal neutron detector array. *Nucl. Instrum. Methods Phys. Res. Sect. A Accel. Spectrometers Detect. Assoc. Equip.* **2019**, *946*, 162639. [[CrossRef](#)]
87. Duclaux, L.; Nysten, B.; Issi, J.P.; Moore, A.W. Structure and low-temperature thermal conductivity of pyrolytic boron nitride. *Phys. Rev. B* **1992**, *46*, 3362. [[CrossRef](#)]
88. Du, X.Z.; Li, J.; Lin, J.Y.; Jiang, H.X. The Origin of Deep-Level Impurity Transitions in Hexagonal Boron Nitride. *Appl. Phys. Lett.* **2015**, *106*, 021110. [[CrossRef](#)]
89. Doan, T.C.; Li, J.; Lin, J.Y.; Jiang, H.X. Bandgap and Exciton Binding Energies of Hexagonal Boron Nitride Probed by Photocurrent Excitation Spectroscopy. *Appl. Phys. Lett.* **2016**, *109*, 122101. [[CrossRef](#)]

90. Spieler, H.G.; Haller, E. Assessment of Present and Future Large-Scale Semiconductor Detector Systems. *IEEE Trans. Nucl. Sci.* **1985**, *32*, 419–426. [[CrossRef](#)]
91. Many, A. High-Field Effects in Photoconducting Cadmium Sulphide. *J. Phys. Chem. Solids* **1965**, *26*, 575–578. [[CrossRef](#)]
92. Maity, A.; Grenadier, S.J.; Li, J.; Lin, J.Y.; Jiang, H.X. Effects of Surface Recombination on the Charge Collection in H-BN Neutron Detectors. *J. Appl. Phys.* **2019**, *125*, 104501. [[CrossRef](#)]
93. Cao, X.K.; Clubine, B.; Edgar, J.H.; Lin, J.Y.; Jiang, H.X. Two-Dimensional Excitons in Three-Dimensional Hexagonal Boron Nitride. *Appl. Phys. Lett.* **2013**, *103*, 191106. [[CrossRef](#)]
94. Doan, T.C.; Li, J.; Lin, J.Y.; Jiang, H.X. Response of Alpha Particles in Hexagonal Boron Nitride Neutron Detectors. *Appl. Phys. Lett.* **2017**, *110*, 213502. [[CrossRef](#)]
95. Dahal, R.; Ahmed, K.; Woei Wu, J.; Weltz, A.; Jian-Qiang Lu, J.; Danon, Y.; Bhat, I.B. Anisotropic Charge Carrier Transport in Free-Standing Hexagonal Boron Nitride Thin Films. *Appl. Phys. Express* **2016**, *9*, 065801. [[CrossRef](#)]